Modelling the Age-Hardening Precipitation by a Revised Langer and Schwartz Approach with Log-Normal Size Distribution

DONGDONG ZHAO, YIJIANG XU, SYLVAIN GOUTTEBROZE, JESPER FRIIS, and YANJUN LI

A new numerical modelling approach integrating the Langer and Schwartz approach and log-normal particle size distribution has been developed to depict the precipitation kinetics of age-hardening precipitates in Al alloys. The modelling framework has been implemented to predict the precipitation behavior of the key secondary phases in 6xxx and 7xxx Al alloys subjected to artificial aging. The simulation results are in good agreement with the available experimental data in terms of precipitate number density, radius, and volume fraction. The initial shape parameter of the log-normal size distribution entering the modeling framework turns to play an important role in affecting the later-stage evolution of precipitation. It is revealed that the evolution of size distribution is not significant when a small shape parameter is adopted in the modelling, while an initial large shape parameter will cause substantial broadening of the particle size distribution during aging. Regardless of the magnitude of shape parameter, a broadening of the particle size distribution as predicted by the present model is in agreement with experimental observations. It is also shown that large shape parameter will accelerate the coarsening rate at later aging stage, which induces fast decreasing of number density and increased growth rate of mean/critical radius. A comparison to the Euler-like multi-class approach demonstrates that the integration of more realistic log-normal distribution and Langer and Schwartz model make the present modelling faster and equivalently accurate in precipitation prediction.

https://doi.org/10.1007/s11661-020-05879-x

I. INTRODUCTION

THE nucleation and growth kinetics of secondary phases during artificial aging heat treatment are crucial in enhancing the mechanical properties of various alloy systems.[1–6] 6xxx and 7xxx aluminium alloys can generally be precipitation strengthened *via* artificial aging, wherein complex precipitation of multiple precipitates occurs, contributing to the hardening of the material.[5,7–11] The extent of precipitation strengthening is largely determined by the precipitate shape, size, and number density. Up to now, various modelling approaches have been developed to predict the precipitation behavior of secondary phases during age-hardening process.[8,9,12–25] Based on the classical nucleation and growth theories, these models are able to predict the time evolution of the precipitation of secondary phases during heat treatment.

The modelling approaches as developed so far, which enable the numerical implementation of the classical nucleation and growth theories generally includes the ''mean size approach'' and the ''multi-class approach''.[13,17,19,26–28] The mean size approach, also named as ''mean radius approach'', was originally proposed by Langer and Schwartz (LS model), wherein the steady-state nucleation theory was adopted to compute the time evolution of phase separation in mixtures.[26] An important simplification of the mean size approach is that only the particles with radius $r > r^*$ (r^* is the critical radius) are included as the newly precipitated phase (see the hatched area in Figure 1). Particles with radius $r < r^*$ (see the unhatched area in Figure 1) are considered as unstable and will dissolve into the supersaturated matrix. The LS model was afterwards improved by Kampmann and Wagner *via* replacing the linearized Gibbs–Thomson equation with

DONGDONG ZHAO, YIJIANG XU, and YANJUN LI are with the Department of Materials Science and Engineering, Norwegian University of Science and Technology (NTNU), 7491 Trondheim, Norway. Contact e-mail: yanjun.li@ntnu.no SYLVAIN GOUTTEBROZE is with the SINTEF Industry, Metal Production and Processing, 0314 Oslo, Norway. JESPER FRIIS is with the SINTEF Industry, Materials and Nanotechnology, 7491 Trondheim, Norway.

Manuscript submitted July 1, 2019.
Article published online July 4, 2020

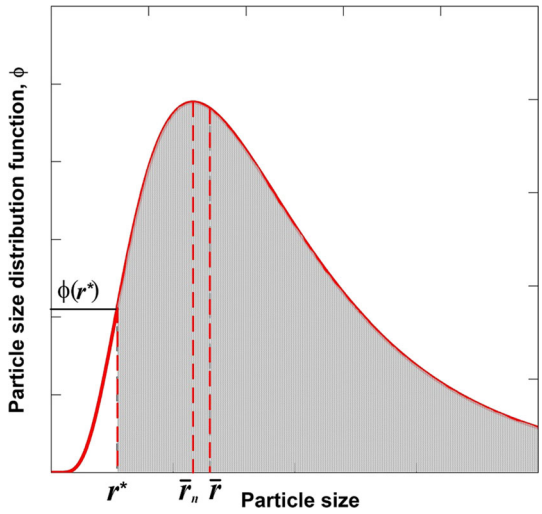

Fig. 1—Log-normal particle size distribution with a mean particle radius $\bar{r}_n$. r^* is the critical radius. Particles with radius $r < r^*$ are continuously dissolving in the matrix. In the present Revised Langer and Schwartz approach, only the hatched area with particle radius $r > r^*$ contributes to the mean particle radius $\bar{r}_n$. $\bar{r}_n$ is the mean radius for the full log-normal distribution and $\bar{r}$ is the mean radius of the stable particles ($r > r^*$).

a non-linearized counterpart (MLS model).[17,29] As being the "mean size approach", both the LS model and MLS model cannot predict the explicit particle size distribution (PSD).

Unlike the "mean size approach", the "multi-class approach" is developed with a definition of discrete size classes and a partitioning of the temporal evolution of PSD into series of individual time steps,[17,29] and hence is able to predict more information about particles, especially the full evolution of PSD. The Kampmann and Wagner numerical model (KWN model) is widely recognized as the pioneering multi-class approach. The KWN model is afterwards improved by Myhr and Grong[13] *via* allowing for the inter-fluxes between neighboring size classes, which is later on named as the "Euler-like multi-class approach". In contrast, the "Lagrange-like multi-class approach" differs from the Euler-like approach, in that it tracks the time evolution of each size class, without inter-size class flow.[28] It is worth noting that the KWN-based multi-class approach bears a generic and flexible nature, which allows for easy extension. A coupling of the KWN-based multi-class approach with the CALPHAD method enables efficient treatment of the multi-phase precipitation in multi-component systems subjected to different heat treatment conditions.[25] Despite the advantage of KWN-based multi-class approach, its application in certain circumstances is less feasible. For instance, the treatment of complex precipitation behavior near defects like grain boundaries or dislocations *via* KWN multi-class approach is not affordable, since one has to discretize the defect region to consider the solute concentration variation. The implementation of KWN multi-class approach in each discrete element turns to make the modeling framework remarkably expensive. A detailed comparison between the mean size and multi-class approaches conducted by Perez *et al.*[19] reveals that in simple cases, the "mean size approach" is faster and as accurate as the multi-class approaches in predicting the general course of precipitation: nucleation, growth, coarsening. This suggests that the "mean size approach" is also able to predict equally accurate results in the modeling framework wherein an implementation of KWN multi-class approach is not computationally affordable.

In spite of the incapability in prediction of PSD evolution, the "mean size approach" still has a wide range of applications, due to its versatility and much less computing load compared with the multi-class approaches. *Via* a "mean size approach" integrating nucleation, growth and coarsening, Deschamps and Bréchet[12] have investigated the effect of predeformation on the precipitation kinetics of an Al-Zn-Mg alloy during aging. A coarsening rate as a function of mean and critical radius was introduced to weigh the pure growth equation and pure coarsening equation to ensure the continuity from growth to coarsening stage. Perrard *et al.*[18] adopted the same approach with a modified coarsening rate to model the precipitation of NbC on dislocations in α-Fe. It is worth noting that these two typical works both have implemented the Lifshitz-Slyozov-Wagner (LSW) kinetics[30] for describing coarsening.[12,18] However, it is demonstrated by Perez *et al.*[19] that the "mean size approach" based on LSW theory is incapable of modelling the PSD evolution of non-LSW precipitation. Meanwhile, the powerful multi-class KWN approaches which can predict PSD evolution also end up with a LSW particle size distribution at long aging time.[13,19,23] However, experimental data does not show characteristic LSW size distribution of precipitates, whereas a log-normal size distribution is commonly observed. Indeed, all the three classic approaches mentioned above cannot properly address the experimental log-normal PSD. These concerns motivate the present research efforts to develop an optimized modelling framework which simply imposes the realistic log-normal size distribution function commonly observed in experiments.

In the present work, we present a revised Langer-Schwartz (RLS) model, which integrates the LS approach and log-normal particle size distribution to depict the precipitation kinetics including nucleation, growth and coarsening. The rest of the manuscript will be arranged as follows. First, the methodologies formulating the present modelling framework, which includes classic nucleation and growth theory, LS approach, log-normal distribution, and solubility product, will be presented in Section II. Hereafter, the numerical precipitation model is applied to treat the nucleation, growth, and coarsening behavior of the key precipitates in 6xxx and 7xxx alloys during aging. The simulation results will be presented and discussed in Section III and IV, followed by the conclusions in Section V.

II. PRECIPITATION MODEL

Prior to a comprehensive introduction of the RLS approach, it is necessary to present the hypotheses adopted in this model:

(i) For simplification of the model, precipitates are assumed to be spherical.
(ii) The thermodynamics of precipitates are described by the solubility product.
(iii) The precipitation reaction, including growth and dissolution, is only controlled by solute diffusion in matrix.
(iv) Local equilibrium at the precipitate/matrix interface is assumed, wherein the Gibbs–Thomson effect is implemented.
(v) An initial constant shape parameter of the log-normal particle size distribution is assumed at the beginning of precipitation.

A. *Nucleation*

The classic nucleation theory is employed to depict the formation of precipitates in supersaturated solid solution. Within this theory, the nucleation rate is calculated in terms of References 31 through 33:

$$J = N_0 Z \beta^* \exp\left(-\frac{\Delta G^*}{k_B T}\right) \exp\left(-\frac{\tau}{t}\right) \quad [1]$$

wherein N_0 is the number of nucleation sites per unit volume, k_B the Boltzmann factor and T the temperature. Z is the Zeldovich factor and is calculated *via*[19]

$$Z = \frac{v_{at}^P}{2\pi r^{*2}} \sqrt{\frac{\gamma}{k_B T}}, \quad [2]$$

where v_{at}^P is the mean atomic volume for the precipitate and γ is the interfacial energy. β^* represents the condensation rate of solute atoms into a cluster with critical size r^*, which can be evaluated based on Russell's equation[34]

$$\beta^* = \frac{4\pi r^{*2}}{a^4} \left(\sum_i \frac{1}{D_i x_i}\right)^{-1} \quad [3]$$

where x_i and D_i are the concentration and diffusion coefficients of solute element i, respectively. Note that ΔG^* is the nucleation energy barrier which needs to be overcome to form a nucleus with size r^*, which is obtained by

$$\Delta G^* = \frac{16\pi\gamma^3}{3\Delta G_v^2}, \quad [4]$$

wherein ΔG_v is the driving force for nucleation per unit volume, which is related to the critical radius r^* *via* interfacial energy γ as

$$r^* = \frac{2\gamma}{\Delta G_v}. \quad [5]$$

Finally, τ in Eq. [1] is the incubation time for nucleation introduced by Kampmann and Wagner,[27] and can be calculated as

$$\tau = \frac{4}{2\pi\beta^* Z^2} \quad [6]$$

B. *RLS Approach*

Within the RLS modelling framework, the instantaneous evolution of the particle number density, particle mean radius, volume fraction, solute concentration in matrix etc. are depicted *via* differential equations. The evolution of the size distribution is given by the following continuity equation

$$\frac{\partial \phi(r)}{\partial t} = -\frac{\partial}{\partial r}(v(r)\phi(r)) + j(r) \quad [7]$$

where v is the particle growth rate, $j(r)$ is the distributed nucleation rate, and $\varphi(r)$ is the log-normal particle size distribution function, which will be presented in the next section. Recognizing that only particles with radius $r > r^*$ are counted into the number density n, we can get the time evolution of n through integrating Eq. [7], leading to

$$\frac{\partial n}{\partial t} = J - \phi(r^*)\frac{\partial r^*}{\partial t} \quad [8]$$

J is the nucleation rate. The mean radius of the particle $\bar{r}$. are defined by

$$\bar{r} = \frac{1}{n}\int_{r^*}^{\infty} \phi(r) r dr \quad [9]$$

By applying the previously defined assumptions, the time derivative of Eq. [9] gives us the time evolution of $\bar{r}$.

$$\frac{\partial \bar{r}}{\partial t} = v(\bar{r}) + \frac{1}{n}\cdot(\bar{r} - r^*)\phi(r^*)\frac{\partial r^*}{\partial t} + \frac{1}{n}\cdot J \cdot (r^* + \delta r^* - \bar{r}), \quad [10]$$

wherein the first term on the right of Eq. [10], $v(\bar{r})$ is the approximation for the growth rate of particles, which can be described with the classic Zener equation.[35] The second term corresponds to the change of $\bar{r}$ contributed by dissolution of $\varphi(r^*)dr^*$ particles with radius $r^* + dr^* > r > r^*$. The third term denotes the change of $\bar{r}$ induced by the nucleation of particles which have radii slightly larger than r^*.

C. *Log-Normal Distribution*

In order for the RLS model to describe the full solution of coarsening of particles in later aging stage, a continuous size distribution function $\varphi(r)$ is needed. Different from previous LS models, we assume a

log-normal distribution of particle sizes for size distribution function $\varphi(r)$ in the present work. Such assumption is feasible and sensible since the log-normal distribution of particle sizes has been frequently observed in various experiments. An implementation of log-normal size distribution for $\varphi(r)$ enable the present RLS model to capture the experimental results in a more realistic manner. The log-normal distribution function $\varphi(r)$ is defined in terms of the following

$$\phi(x) = \frac{1}{\sqrt{2\pi}sx}\exp\left(-\frac{\left(\ln x + s^2/2\right)^2}{2s^2}\right), \qquad [11]$$

wherein x is the normalized particle size for size class i with respect to the mean particle radius, *i.e.*, $r_i/\bar{r}$. s is the shape parameter for the $\varphi(r)$, which has the term of the following

$$s^2 = \ln\left(1 + \frac{\sigma_r^2}{\bar{r}^2}\right), \qquad [12]$$

where σ_r is the measured standard deviation of the experimental precipitate size distribution. A normalized distribution function with respect to the normalized particle size is shown in Figure 2. As one can find that log-normal PSD with larger shape parameter would correspond to a more broader distribution.

D. *Growth Rate*

The classical diffusion-controlled growth rate equation[35] has been adopted to describe both particle dissolution and growth in the differential equations, which is termed as

$$v = \frac{dr}{dt} = \frac{D_j}{r}\frac{\bar{x}_j - x_j^i(r)}{\alpha x_j^p - x_j^i(r)}, \qquad [13]$$

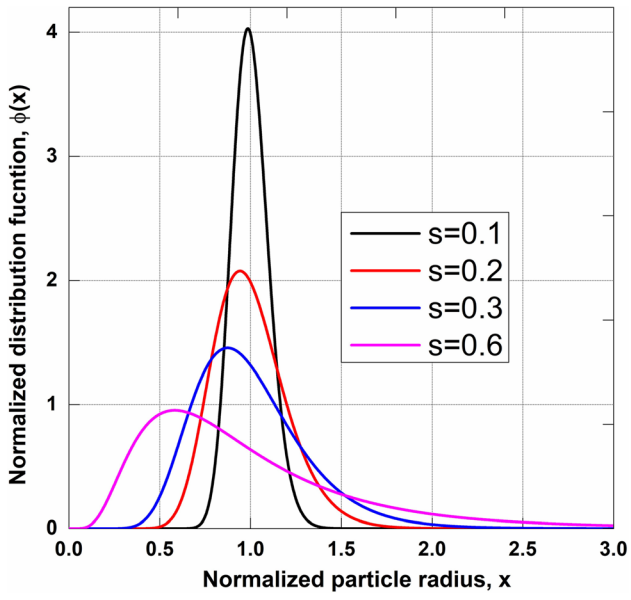

Fig. 2—Log-normal particle size distribution with four different shape parameters (0.1, 0.2, 0.3, 0.6).

wherein D_j is the solute diffusion coefficient in matrix, r the spherical particle radius, the mean solute concentration in matrix, the solute concentration in precipitate, the solute concentration at the particle/matrix interface. $\bar{x}_j$, x_j^p, and $x_j^i(r)$ are the solute concentrations of element j in the matrix, the particles and at the particle/matrix interface, respectively. α is the ratio between mean atomic volume of matrix and precipitate.

Local equilibrium of the solute concentration at the particle/matrix interface is assumed *via* the Gibbs–Thomson effect, which can be described by the following equation with the solubility product (considering A_mB_n precipitate)[36]:

$$K(r) = \left(x_A^i\right)^m\left(x_B^i\right)^n = K^\infty \exp\left(\frac{2\gamma V_m}{rRT}\right), \qquad [14]$$

wherein γ is the particle/matrix interfacial energy and x_A^i, x_B^i represent the solute concentration at the particle/matrix interface of element A and B, respectively. K^∞ is the equilibrium solvus boundary, given by,

$$K^\infty = \left(x_A^\infty\right)^m\left(x_B^\infty\right)^n = \exp\left(\frac{\Delta S^\circ}{R} - \frac{\Delta H^\circ}{RT}\right), \qquad [15]$$

where x_A^∞ and x_B^∞ are the equilibrium concentration of the solute elements, respectively. ΔS° and ΔH° are the formation entropy and enthalpy of the precipitate. Note that K^∞ is only valid for a particle with infinite size. The driving force for nucleation can then be given by[37]

$$\Delta G_v = RT \cdot \ln\left[\left(\bar{x}_A\right)^m\left(\bar{x}_B\right)^n\right] - \left(\frac{\Delta S^\circ}{R} - \frac{\Delta H^\circ}{RT}\right) \qquad [16]$$

The critical size r^* of the particles can be determined when the growth rate v (Eq. [13]) is zero, wherein the solute mean concentration equals to the solute interfacial concentration,

$$\bar{x}_A = x_A^i(r),\ \bar{x}_B = x_B^i(r) \qquad [17]$$

Substituting Eq. [17] into Eq. [14], we can get the critical radius r^* for the particles.

$$r^* = \frac{2\gamma V_m}{RT \cdot \ln\left[\left(\bar{x}_A\right)^m\left(\bar{x}_B\right)^n\right] - \left(\frac{\Delta S^\circ}{R} - \frac{\Delta H^\circ}{RT}\right)} \qquad [18]$$

A basic assumption in the present precipitation model is that the growth rate is diffusion-controlled. In multi-component systems, we have multiple growth rate equations for the precipitate as a result of the different solute elements. By assuming the same overall growth rate regardless of which element is considered, we have the following (considering A_mB_n precipitate)

$$\frac{D_A}{r}\frac{\bar{x}_A - x_A^i(r)}{\alpha x_A^P - x_A^i(r)} = \frac{D_B}{r}\frac{\bar{x}_B - x_B^i(r)}{\alpha x_B^P - x_B^i(r)} \qquad [19]$$

Solving Eqs. [14] and [19], the solute concentrations at the particle/matrix interface and the growth rate can be

determined. Mass balance is calculated to update the solute concentration in the matrix as the precipitation is proceeding, which can be evaluated by

$$\bar{x}_i = \frac{\overline{x_i^0}(1 + \alpha f_v - f_v) - \alpha x_i^P f_v}{1 - f_v} \quad [20]$$

where f_v is the particle volume fraction.

III. APPLICATIONS

A. *Model Prediction of β″ Precipitation*

The precipitation kinetics of 6xxx alloys subjected to artificial aging is rather complex, which involves multiple secondary phase precipitation, including pre-β″, β″, B′, β′, U1, U2, and the stable β precipitates. It is well established that the β″ phase with a needle morphology is the most effective strengthening precipitate. The present modeling framework is utilized to predict the precipitation of β″ in an Al-0.52 Mg-0.75Si (in wt pct) alloy during aging treatment, and the experimental data describing the precipitation behavior of β″ are from Reference 23. The classical nucleation theory is intrinsically sensitive to the particle/matrix interfacial energy γ, which makes this parameter crucial for the present modelling prediction. The γ of β″/Al-matrix interface is difficult to determine due to its dependency on precipitate size and interfacial anisotropy.[2,38] As an early stage metastable precipitate, the γ of β″/Al-matrix interface is considered small as a result of a full coherency of β″ with the Al matrix along the precipitate needle direction and semi-coherency along ***a*** and ***c*** axes. In the present simulation, a value of 0.05 J/m^2 for γ was adopted, which is very close to the value of 0.045 J/m^2 utilized in Du's multi-class approach.[23] Note that a stoichiometry of Mg_5Si_6 is implemented for the β″ phase. Other key parameters for modelling precipitation of β″ are summarized in Table I.

Figure 3 displays the predicted number density, mean/critical radius, and volume fraction of β″-Mg_5Si_6 precipitate as a function of aging time. The experimental results based on transmission electron microscopy (TEM) measurements from Du *et al.*,[23] are also plotted for comparison. As one can find in Figure 3(a) that the present modelling can well capture the number density evolution of β″-Mg_5Si_6, both at peak hardening and later over aging stage. Du *et al.*,[23] have shown that their KWN multi-class model in combination with spherical particle assumption is unable to well predict the number density evolution of β″-Mg_5Si_6 especially at later aging stage. It was demonstrated that a consideration of the non-spherical shape with an aspect ratio can effectively enhance the coarsening rate and hence increase the model capability. The present modelling framework is considered very promising given the fact that it can well depict the number density evolution even with spherical particle assumption. Figure 3(b) shows the time evolution of mean and critical radius of β″-Mg_5Si_6 particles in comparison with the experimental data. The predicted mean radius is in good agreement with experimental results at early aging stage (3, 36 hours), but bears discrepancy with experiment at late aging stage (108 hours). This may be attributed to the phase transformation of age-hardening precipitates. After a long time artificial aging, the dominant precipitate will become β′ instead of β″, which is beyond the prediction ability of the present model. Better prediction might be achieved by taking into account the precipitation of β′ precipitate in the later aging stage. It is shown in Figure 3(c) that the predicted volume fraction of β″-Mg_5Si_6 precipitates is in less agreement with the experimental results, especially after 10^5 seconds artificial aging, the predicted values are much smaller than that measured. Similar disagreement was also observed in between the predicted and measured volume fractions by KWN multi-class approach.[23] Note that both models implemented a stoichiometry of Mg_5Si_6 for β″, which has been recently established to have a constitution of $Al_2Mg_5Si_4$.[39] This can be one reason leading to the lower predicted volume fraction of precipitates. Moreover, the sudden increase in measured volume fraction of early-stage β″ at later aging stage determined by experiments is quite unlikely to occur. It is considered that the volume fraction may include contributions from precipitates at later aging stage, which contains transformation of precipitates and is beyond the prediction ability of the present modeling. Figure 3(d) shows the time evolution of the mean concentration of Mg, Si solute in the matrix. Significant decrease of the Mg, Si concentration in matrix are accompanied with the substantial nucleation (*cf.* Figure 3(a)) and increased volume fraction (*cf.* Figure 3(c)) of β″ precipitates at the timescale of 10^3 to 10^4 seconds before reaching the solubility limit leading to a slow increase of the volume fraction during coarsening.

Table I. Key Input Parameters for the Precipitation Modelling of β″ in an Al-0.52 Wt Pct Mg-0.75 Wt Pct Si Alloy

Parameter	Value
Molar Volume of Al Matrix	1.0×10^{-5} m^3/mol
Molar Volume of β″ Precipitate	1.092×10^{-5} m^3/mol
Interfacial Energy, γ	0.05 J/m^2
Diffusion Mobility of Mg in Matrix[49]	1.342×10^{-19} m^2/s
Diffusion Mobility of Si in Matrix[49]	2.706×10^{-19} m^2/s
Shape Parameter of Log-Normal PSD	0.03
Solvus Boundary	from Ref. [50]

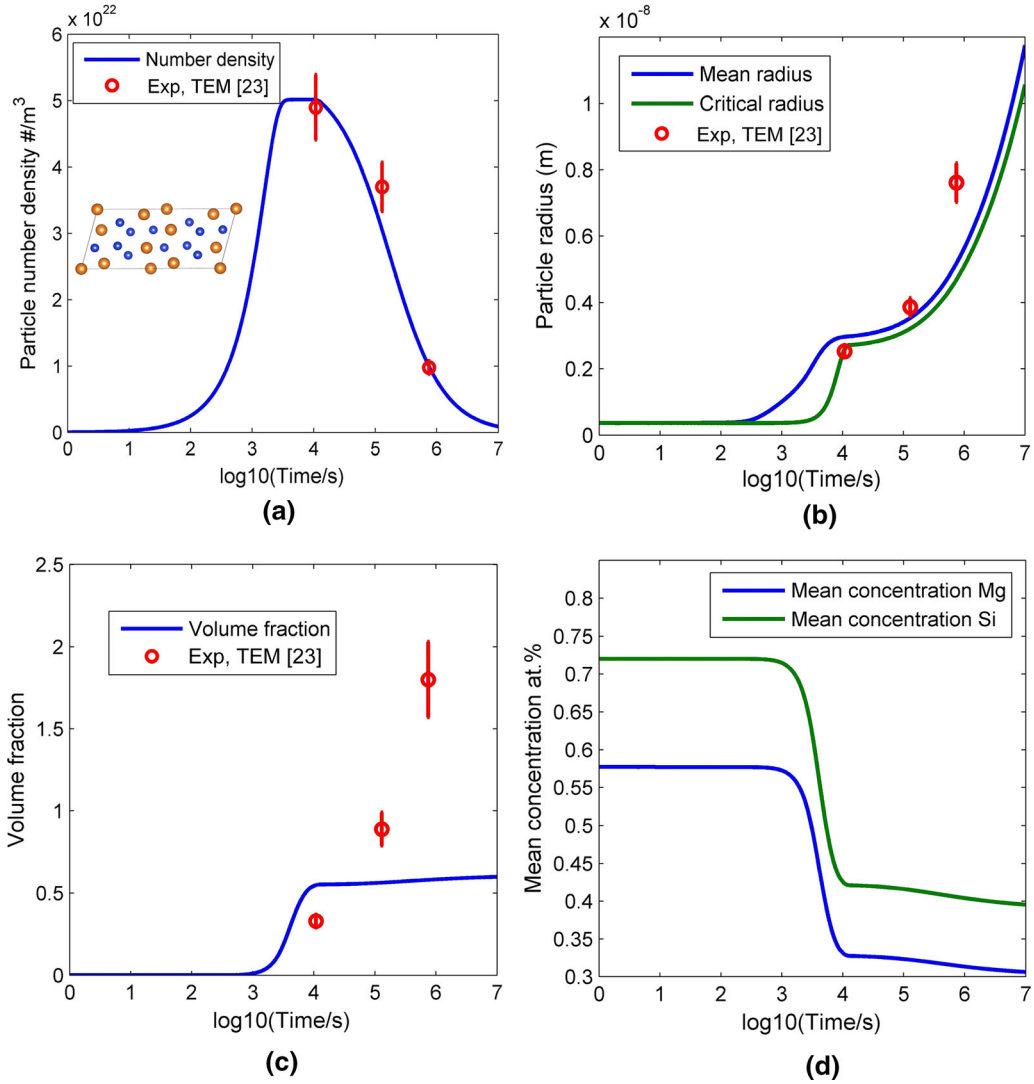

Fig. 3—Predicted time evolution of (*a*) β''-Mg_5Si_6 precipitate number density, (*b*) precipitate radius, including mean and critical radius, (*c*) precipitate volume fraction, (*d*) mean concentration of Mg, Si solute in the matrix in an Al-0.52Mg-0.75Si alloy during artificial aging at 175 °C. The experimental results from Ref. [23] are also plotted for comparison.

B. *Model Prediction of β' Precipitation*

β' is a later-stage precipitate of 6xxx alloys during artificial aging. This phase, possessing a rod morphology, has a hexagonal unit structure with space group of $P6_3/m$. The precipitation behavior of β' phase in a commercial 6056 Al alloy[41] during artificial aging is utilized to validate the present precipitation model. As discussed above, the interfacial energy γ would drastically affect the nucleation rate and hence number density. The β' precipitate is solely coherent with the Al matrix along the ***c*** axis, which is less coherent in comparison with the β''/Al-matrix interface. Hence, a higher interfacial energy γ for β'/Al-matrix interface can be expected. A reasonable γ value of 0.08 J/m^2 which enables a good prediction of the β' precipitation behavior has been used in the present work. Note that this value is a bit smaller than the interfacial energy (0.104 to 0.112 J/m^2) adopted in the multi-class Lagrangian-like modelling of β' precipitation by Bardel *et al.*[8] The stoichiometry of Mg_9Si_5 established by Vissers *et al.*[40] is used for the β' precipitation modelling. The other key parameters for modelling precipitation of β' are summarized in Table II.

Figure 4 shows the predicted number density, mean/critical radius, and volume fraction of β'-Mg_9Si_5 precipitate *vs* time evolution. The experimental information of the β' precipitate from the characterization of 6056 alloy subjected to T6 temper treatment by Donnadieu *et al.*[41] are also included in the figures for comparison. It can be seen in Figure 4 that the model predictions are well consistent with the TEM experimental measurements of β' precipitation, both in number density, particle size, and volume fraction at the aging time of 8 hours. A comparison between Figures 3 and 4 enables one to find that the predicted coarsening rate of β'' is much faster than β' at the late aging stage. Such higher coarsening rate of β'' seems to be in contradiction with its smaller interfacial energy than β',

Table II. Key Input Parameters for the Precipitation Modelling of β' in a Commercial 6056 Aluminium Alloy

Parameter	Value
Molar Volume of Al Matrix	1.0×10^{-5} m^3/mol
Molar Volume of β' PRECIPITATE	1.124×10^{-5} m^3/mol
Interfacial Energy, γ	0.08 J/m^2
Diffusion Mobility of Mg in MATRIX[49]	1.342×10^{-19} m^2/s
Diffusion Mobility of Si in Matrix[49]	2.706×10^{-19} m^2/s
Shape Parameter of Log-Normal PSD	0.01
Solvus Boundary	from Ref. [50]

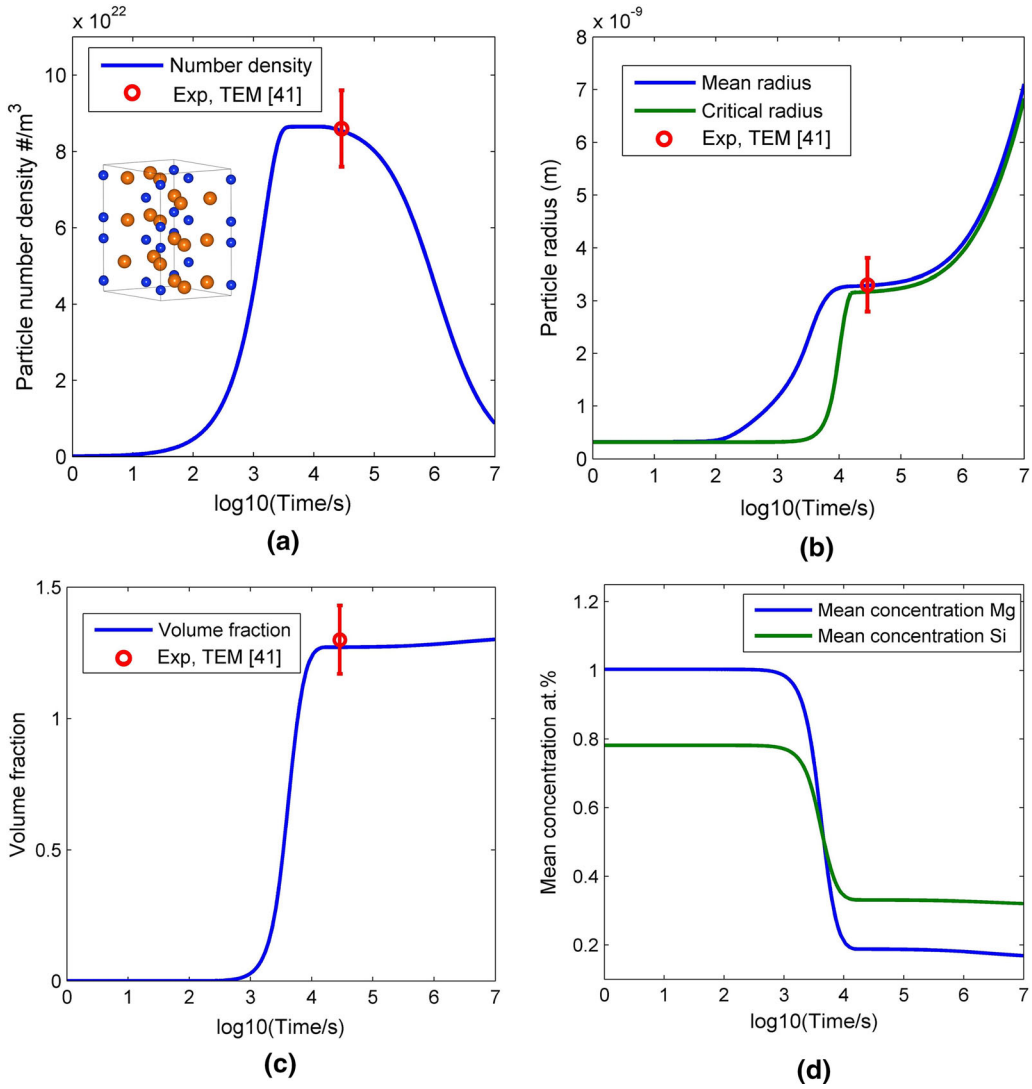

Fig. 4—Predicted time evolution of (*a*) β'-Mg_9Si_5 precipitate number density, (*b*) precipitate radius, including mean and critical radius, (*c*) precipitate volume fraction, (*d*) mean concentration of Mg, Si solute in the matrix in 6056 alloy during artificial aging at 175 °C. The experimental results from Ref. [41] are also plotted for comparison.

which turns to slow down the growth rate of β''. However, the coarsening behavior of the precipitate is not solely controlled by the interfacial energy. According to Eq. [10], an increase of the mean particle radius is contributed by the Zener growth equation and dissolution of particles with instantaneous radius smaller than r^* at late aging (coarsening) stage, wherein the nucleation rate at this stage is approaching ~0, with no contribution of newly nucleated particles to mean particle radius. As a result of the same aging temperature, the diffusion controlled Zener growth equation is not supposed to cause large discrepancy in the growth

rate of the two precipitates. On the contrary, the dissolution of particles with radius $r < r^*$ should play a deterministic role in the coarsening rate. One can clearly find in Eq. [18] that multiple factors rather than sole interfacial energy will serve to determine the critical radius, including precipitate molar volume, solute mean concentration, and solvus boundary. The different time evolution of the critical radius r^* causes the distinct coarsening rate between β'' and β' as predicted in the present modelling.

C. *Model Prediction of η' Precipitation*

The generic precipitation sequence of an Al-Zn-Mg alloy during artificial aging is widely recognized as: solid solution $\rightarrow$ GP zones $\rightarrow$ metastable $\eta' \rightarrow$ stable η, wherein the η' precipitates serve as the major secondary phases contributing to the age-hardening of Al-Zn-Mg alloy.[42] For the sake of predicting the η' precipitation behavior, a stoichiometry of $Mg_4Zn_{11}Al_1$ has been adopted in the present modelling. Such stoichiometry is based on the atomic model of η' phase established by Auld and Cousland,[43] which has been validated by Wolverton[44] using density functional theory (DFT) calculations. It is worth noting that the η'/matrix interfaces are also anisotropic, wherein the $\{0001\}_{\eta'}/\{111\}_{Al}$ interface is coherent, while the $\{10-10\}_{\eta'}/\{110\}_{Al}$ interface is semi-coherent. This makes it difficult to precisely determine the η'/matrix interfacial energy. Based on DFT, Cao *et al.*[45] have predicted interfacial energies of ~44 and 190 mJ/m^2 for the coherent and semi-coherent interfaces, respectively. Hence in the present work, an optimal value of 0.1 J/m^2 has been used. Such interfacial energy is larger than the value of 0.06 J/m^2 adopted by Kamp *et al.*[46] to predict the precipitation and dissolution of η' phase during friction stir welding process. The other key parameters adopted for modelling η' precipitation are as tabulated in Table III.

The predicted time evolution of number density, mean/critical radius, and volume fraction for η' precipitates in a 7150 alloy are displayed in Figure 5. The experimentally measured number density, mean/critical radius, and volume fraction at peak-aging time of 24 hours as determined by small-angle X-ray scattering (SAXS) and TEM methods[47] are also included in the figures for comparison. It is clearly shown in Figure 5 that the present modelling framework can well predict the precipitation behavior of η' phase at the peak-aging stage. Note that the peak hardening of 7xxx alloys usually occurs at ~24 hours, being much slower than the peak-hardening time of 6xxx alloys, which can be ascribed to the much lower diffusivity of the impurity elements at lower aging temperature (~120 °C). One can find that the predicted peak hardening occurs in the time range of 10^4 to 10^5 seconds, being consistent with the experimental observations. The lower diffusivity of the solute elements can be reflected by the much lower increasing rate of the mean radius during aging. One can find in Figure 5(b) that corresponding to the peaking particle number density, a substantial increase in mean particle radius also occurs at the timescale of 10^4 to 10^5 seconds, which is much longer than the timescale of 10^3 to 10^4 seconds in 6xxx alloys. Figure 5(e) shows the time-evolution of Al concentration in the matrix. One can find that along with the precipitation of η' phase, there is an increase of the Al contents in the matrix. This is not surprising considering the consumption of Mg, Zn solutes in the matrix due to the continuous nucleation and growth of the η' phase, which induces a monotonic increase of Al content in the matrix according to the conservation law. Figure 6 displays the comparison of predicted properties, *i.e.*, number density, mean radius, volume fraction, of η' precipitate by RLS model with the experimental data measured in six 7xxx alloy systems.[47] The good agreement between the prediction and experimental results as indicated in Figure 6 validates that the RLS model is able to adequately capture the precipitation behaviors of η' phase in these alloys.

The same set of parameters except for the shape parameter as adopted in the present RLS modelling were employed to depict the evolution of η' precipitate radius in an Al-6.1 wt pct Zn-2.35 wt pct Mg model alloy subjected to artificial aging at 160 °C. Note that a different shape parameter of $s = 0.07$ instead of 0.01 was utilized for the precipitation modelling. The effect of this parameter on precipitation behavior will be discussed in a latter section. For the precipitation modelling of target alloy aged at 160 °C with a slow heating rate, an interfacial energy of 0.09 J/m^2 instead of 0.1 J/m^2 (fast heating rate) was implemented, which corresponds to a lower nucleation energy barrier, accounting for the easier nucleation of η' precipitate on GP zone as reported by Deschamps *et al.*[12,48] Figure 7 shows the

Table III. Key Input Parameters for the Precipitation Modelling of η' in an 7150 Alloy

Parameter	Value
Molar Volume of Al Matrix	1.0×10^{-5} m^3/mol
Molar Volume of η' Precipitate	5.384×10^{-6} m^3/mol
Interfacial Energy, γ	0.1 J/m^2
Diffusion Mobility of Mg in Matrix[49]	1.455×10^{-21} m^2/s
Diffusion Mobility of Zn in Matrix[49]	4.464×10^{-21} m^2/s
Shape Parameter of Log-Normal PSD	0.01
Solvus Boundary	From Ref. [44,51]

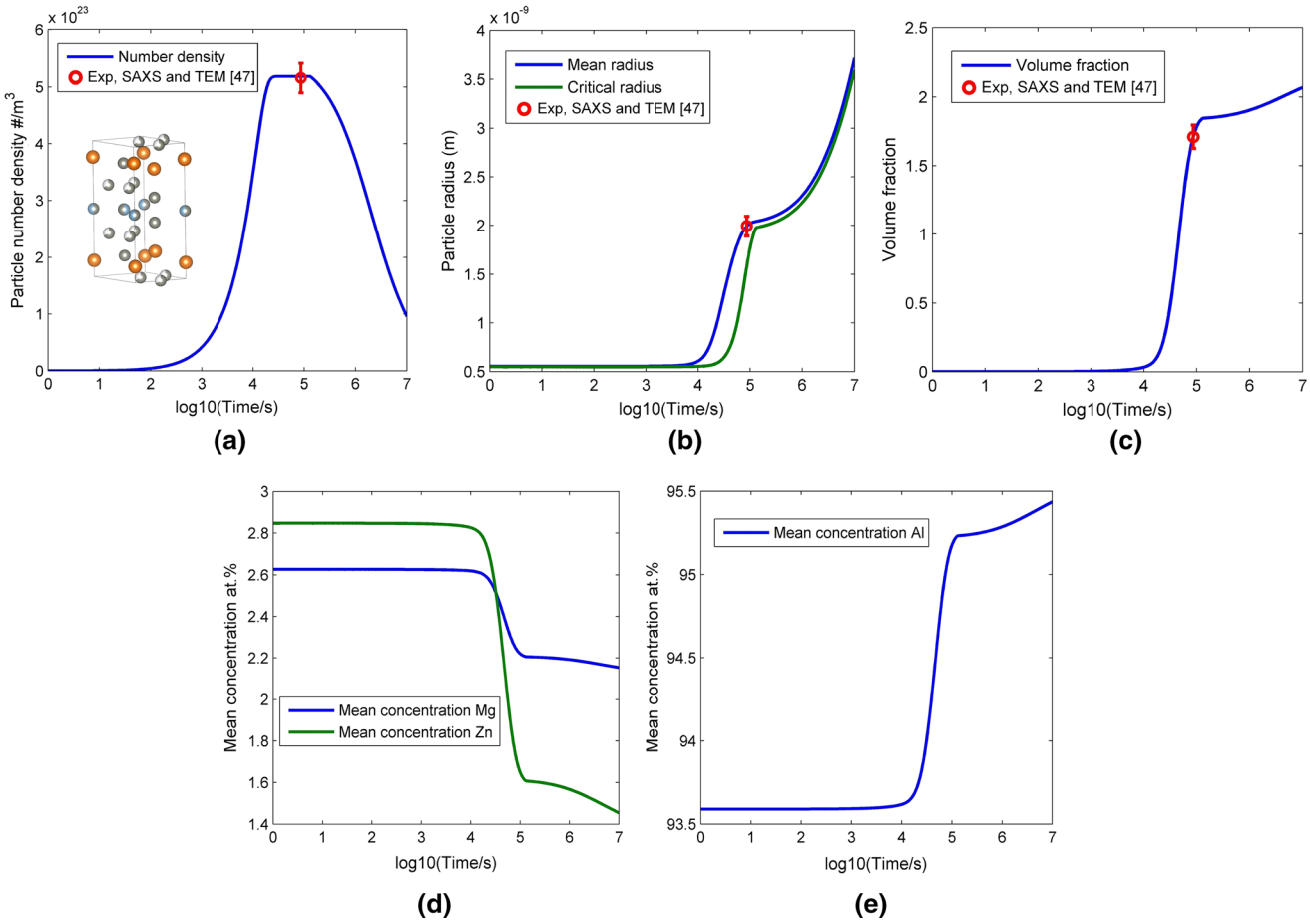

Fig. 5—Predicted time evolution of (*a*) η'-$Mg_4Zn_{11}Al_1$ precipitate number density, (*b*) precipitate radius, including mean and critical radius, (*c*) precipitate volume fraction, mean concentration of (*d*) Mg, Zn, (e) Al solute in the matrix in 7150 alloy. The experimental results from Ref. [47] are also plotted for comparison.

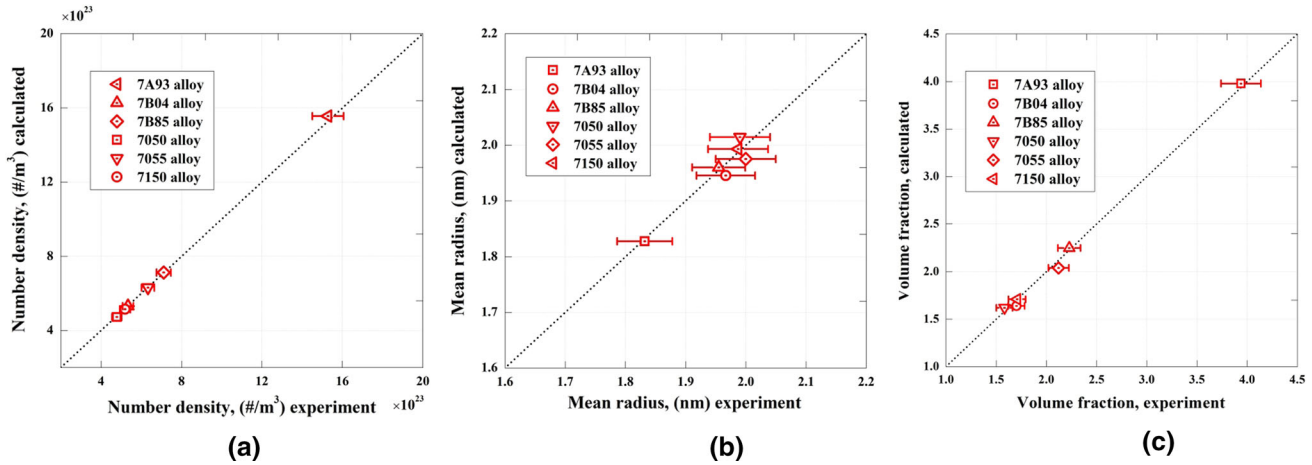

Fig. 6—Predicted properties of η'-$Mg_4Zn_{11}Al_1$ precipitate by the RLS model against the experimental data in six alloy systems from Ref. [47], (*a*) calculated *vs* experimental number density, (*b*) calculated *vs* experimental mean radius, (*c*) calculated *vs* experimental volume fraction.

predicted time evolution of precipitate radius, including mean and critical radius in comparison with the small angle scattering (SAXS) and TEM data.[12,48] As indicated, the present modelling framework can deliver a remarkably accurate prediction of the evolution of precipitate radius throughout the aging process. Besides, at early aging stage, the predicted precipitate radius is slightly smaller than the measured values both in the

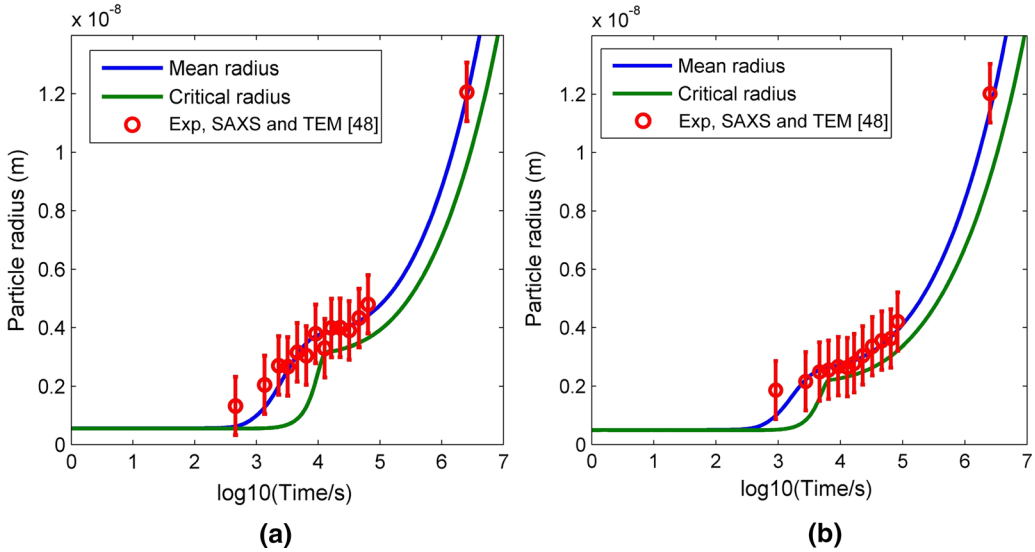

Fig. 7—Predicted time evolution of precipitate radius, including mean and critical radius in comparison with the Small Angle Scattering and TEM data from Ref. [48], (*a*) precipitate radius of Al-Zn-Mg alloy aged at 160 °C with a fast heating rate, (*b*) precipitate radius of Al-Zn-Mg alloy aged at 160 °C with a slow heating rate.

fast- and slow-heating cases. This discrepancy with the experiments can be explained by the presence of GP zone during early aging stage, which contributes to the precipitate radius determined by experiments. However, the predicted precipitate radius in the modelling is only for the η' precipitate, wherein the contribution of GP zone has not been taken into account.

IV. DISCUSSION

A. *Log-Normal Distribution and the Shape Parameter*

As demonstrated, the RLS precipitation model within the framework of mean size approach, is able to accurately describe the precipitation behaviors including nucleation, growth and coarsening of a variety of precipitates during aging treatment. As an important factor entering the RLS modelling framework, the log-normal size distribution has large influence on the predicted precipitation behavior, hence the sensitivity of the model to the key physical parameter describing log-normal size distribution, *i.e.*, shape parameter s, need to be evaluated.

Comparing Figs. 3b, 4b, 5b and 7a and b, one can easily see a correlation between the shape parameter s of the log-normal size distribution and the value difference between $\bar{r}$ and r^* at the coarsening stage. A large shape parameter s would correspond to a large value difference between $\bar{r}$ and r^* at the coarsening stage (Figures 3(b) and 7(a) and (b)). However, a small s would produce a small value difference between the two (Figures 4(b) and 5b). Such behavior can be explained by the intrinsic dispersion feature of the log-normal size distribution. A large shape parameter s describes a broader size distribution, where one could expect a relatively larger difference between $\bar{r}$ and r^*. On the contrary, a narrower size distribution characterized with smaller shape parameter would yield much smaller difference between the two. In turn, the magnitude of value discrepancy between these two parameters at the coarsening stage can also serve as an indication whether there is a large change in the particle size distribution.

Figure 8 displays the effect of shape parameter s of the log-normal distribution on the time evolution of particle radius, including mean/critical radius, and radius difference $\bar{r} - r^*$ for the Q-$Al_3Cu_2Mg_9Si_7$ phase, as predicted by the RLS approach in the present work. The key parameters for modelling precipitation of Q phase are as listed in Table IV. One can clearly identify that a smaller s corresponds to a smaller radius difference between $\bar{r}$ and r^*, and vice versa. It is also shown in Figure 8 that the particle radius difference $\bar{r} - r^*$ at coarsening stage is not a constant, which monotonically increases regardless of the magnitude of the initial shape parameter. This implies that the shape parameter depicting the log-normal distribution is continuously increasing, which refers to a sustained broadening of the size distribution during coarsening stage. Such interesting feature is in good agreement with the results by both experiments and Euler approaches showing clearly an broadening of the particle size distribution during aging especially later stage.[13,23] However, the extent of increment of the radius difference $\bar{r} - r^*$ along with aging time is different in respect to the distinct initial shape parameter. For small s (*cf.* Figure 8(a)), the increase in the radius difference $\bar{r} - r^*$ is quite small even at long aging time (~10^7 seconds), while larger s produce a drastically increased particle radius difference $\bar{r} - r^*$ (*cf.* Figure 8(a)). The magnitude of radius difference $\bar{r} - r^*$ at coarsening stage is demonstrated as being able to identify the broadening/evolution of particle size distribution. Hence, the initial shape parameter s is supposed to play a key role in affecting the later-stage evolution of particle size distribution. It is supposed that the evolution of the size distribution is

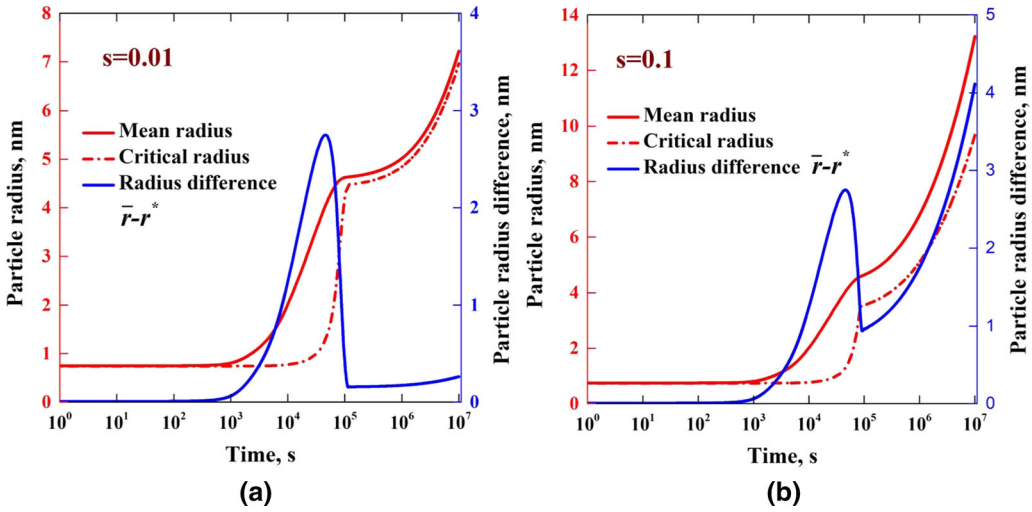

Fig. 8—Effect of shape parameter s = (*a*) 0.01 and (*b*) 0.1 of the log-normal distribution on the time evolution of Q-$Al_3Cu_2Mg_9Si_7$ precipitate radius, including mean/critical radius, and radius difference between $\bar{r}$ and r^*, predicted by the RLS approach in the present work.

Table IV. Key Input Parameters for the Precipitation Modelling of Q-$Al_3Cu_2Mg_9Si_7$ Phase

Parameter	Value
Molar Volume of Al Matrix	1.0×10^{-5} m^3/mol
Molar Volume of η' Precipitate	1.077×10^{-5} m^3/mol
Interfacial Energy, γ	0.16 J/m^2
Diffusion Mobility of Mg in Matrix[49]	1.342×10^{-19} m^2/s
Diffusion Mobility of Si in Matrix[49]	2.706×10^{-19} m^2/s
Diffusion Mobility of Cu in Matrix [49]	1.096×10^{-20} m^2/s
Solvus boundary	from Ref. [52]

not significant during aging when a small shape parameter is selected in the modelling, while an initial large shape parameter will result in a substantial broadening of the particle size distribution.

Indeed, the shape parameter of the log-normal distribution does not solely influences the particle size distribution during precipitation, but also affects the evolution of other parameters during precipitation. Figure 9 shows the effects of shape parameter s of the log-normal distribution on the time evolution of precipitate number density, mean/critical radius, and volume fraction for Q-$Al_3Cu_2Mg_9Si_7$ phase, predicted by the RLS approach in the present work. The different shape parameter s is shown to hardly affect the number density evolution at early and peak-aging stage. However, a larger s can significantly accelerate the coarsening rate at later aging stage, as indicated by the faster decrease in number density with larger s (*cf.* Figure 9(a)). Correspondingly, one can find that the variation of shape parameter does not change the evolution of particle mean/critical radius (*cf.* Figures 9(b) and (c)) at early and peak-aging stage, but a larger s substantially enhances the growth rate of mean/critical radius at later aging stage. This interesting feature can be accounted for using the different log-normal distributions characterized with different shape parameters. As discussed above, an initial large shape parameter will produce continuous broadening of the log-normal distribution during precipitation. A broader size distribution described with a larger s will correspondingly have more particles with radius $r < r^*$ (*cf.* Figure 1), which will dissolve in the solid solution matrix. Such dissolving of the smaller particles will enormously contribute to the coarsening of the larger particles. Hence, a larger shape parameter s will produce faster coarsening rate of the precipitate at later aging stage. Nevertheless, the variation of shape parameter does not induce a significant influence on the volume fraction of the precipitate (*cf.* Figure 9(d)).

B. *Comparison with the Euler-Like Multi-class Approach*

A comparison between the present RLS model with the Euler-like multi-class approach was made in terms of predicted number density, particle radius, volume fraction and solute mean concentration in order for a validation of its accuracy and efficiency. The details of the Euler-like approach can be referred to in References 13 and 19 To facilitate the comparison, the same set of parameters (*cf.* Table IV) were adopted for these two approaches. Figure 10 shows the predicted precipitation results of Q-$Al_3Cu_2Mg_9Si_7$ phase by the two approaches in terms of number density, particle radius, volume fraction and solute mean concentration. Note that a

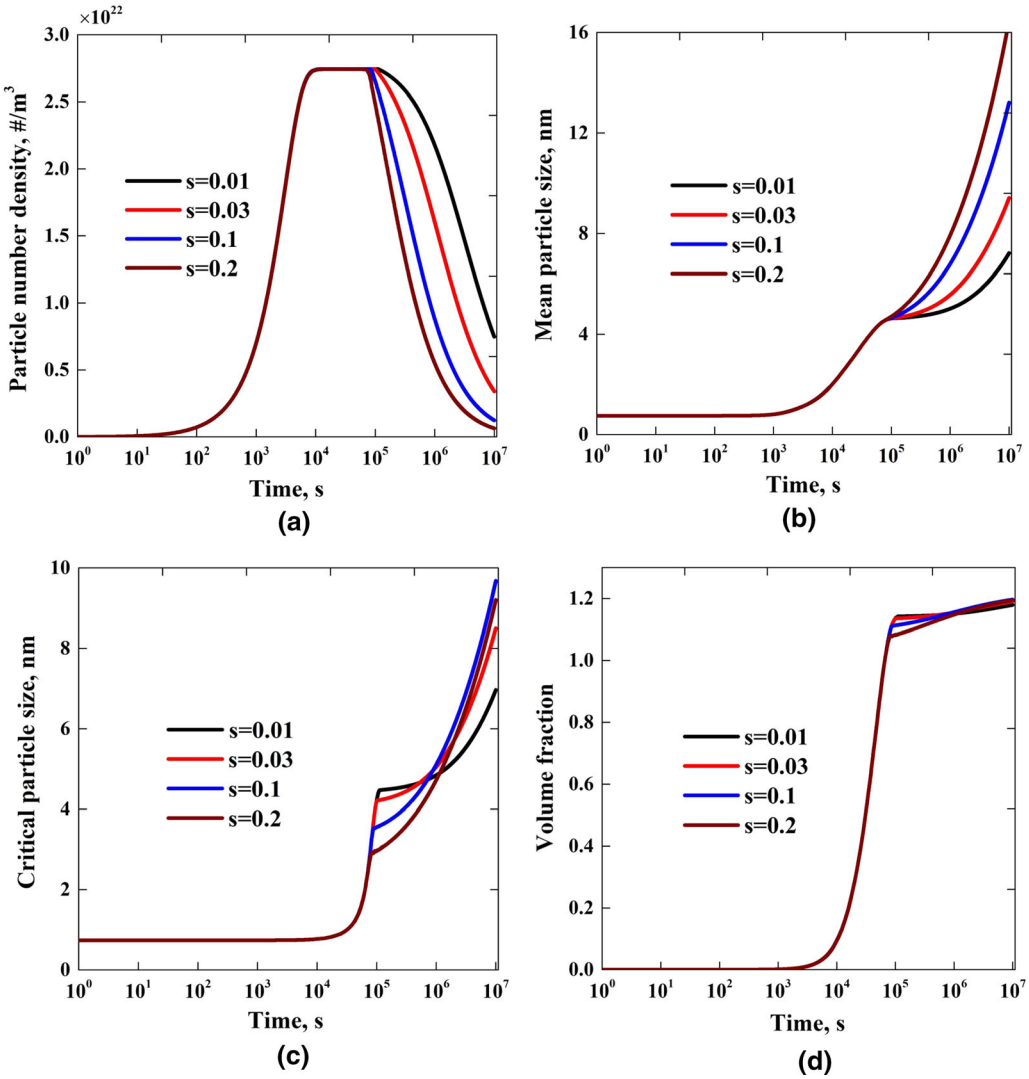

Fig. 9—Effect of shape parameter s of the log-normal distribution on the time evolution of (*a*) Q-$Al_3Cu_2Mg_9Si_7$ precipitate number density, precipitate radius, including (*b*) mean and (*c*) critical radius, (*d*) precipitate volume fraction, predicted by the RLS approach in the present work.

shape parameter of $s = 0.04$ is implemented for the log-normal distribution in the RLS model. One can find that the prediction results of these two approaches are remarkably consistent with each other. The different particle size distributions, *i.e.*, a log-normal distribution as adopted in the RLS approach and a LSW distribution as predicted in the Euler-like approach[13] can be one reason accounting for the slight difference in the evolution of number density and radius between these two approaches. The integration of more realistic log-normal distribution, solubility product and LS model make this approach faster and equivalently accurate in precipitation prediction when compared to the multi-class approaches. Nevertheless, even though a log-normal distribution has been integrated in the RLS approach, the precise prediction of the evolution of particle size distribution is still not possible, which is the intrinsic feature of mean size approaches. It is worth noting that the introduction of the log-normal distribution with an arbitrary shape factor s is an simplification of the real size distribution. Such simplification is hard to relate to the true physics of precipitation at the beginning, since $s = 0$ is when nucleation starts for the first time due to the fact that particles nucleate with the same critical radius r^*. During growth and coarsening at later aging stage, s is increasing as a result of nucleation of new nuclei with larger r^* and the particle growth. Even as a mean size approach, the RLS approach can be promisingly further improved if the evolution of shape parameter s which characterizes the log-normal distribution can be properly addressed in the modelling framework during the precipitation process. Such description for the evolution of shape parameter s is complex and will be reported in our future research work.

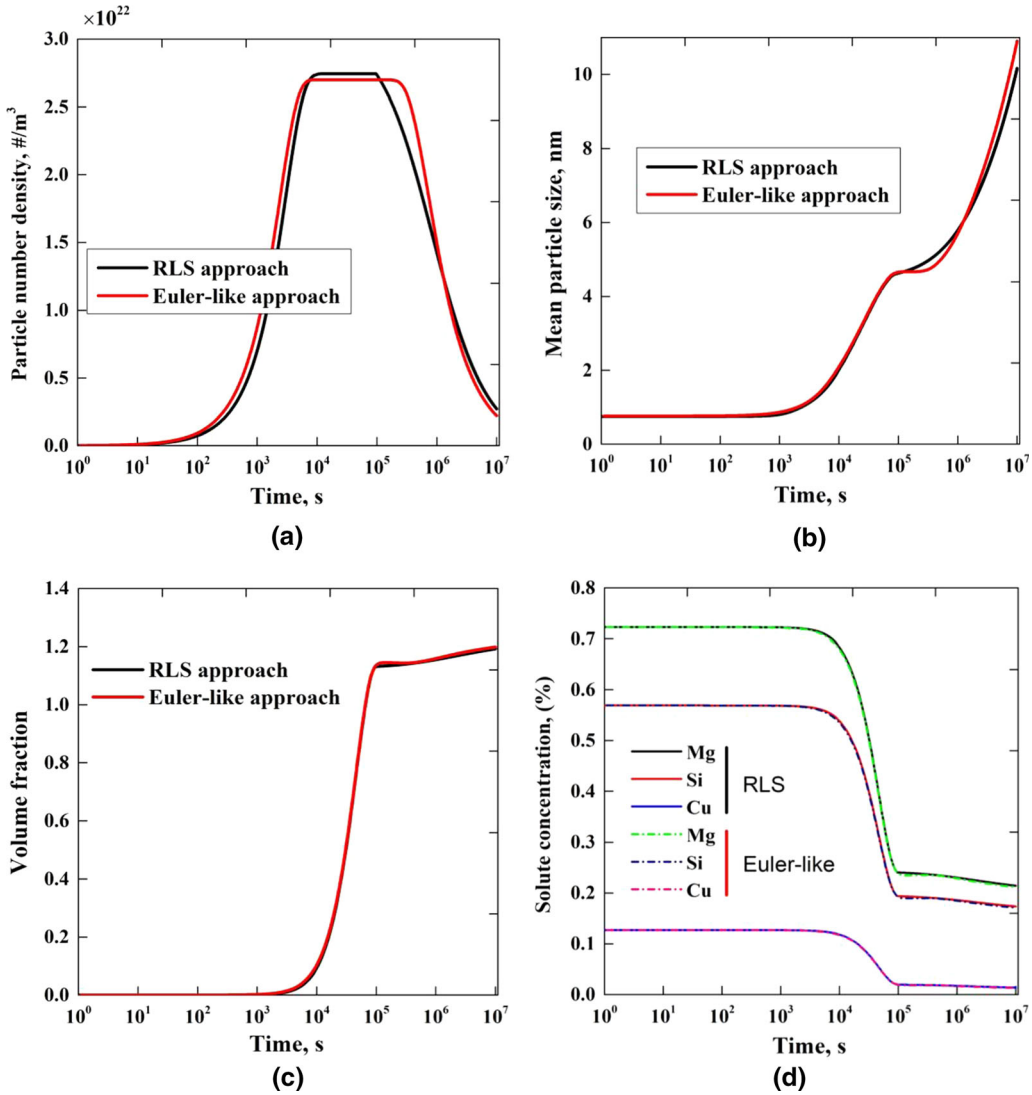

Fig. 10—Predicted time evolution of the (*a*) particle number density, (*b*) mean particle radius, (*c*) precipitate volume fraction, and (*d*) solute concentration in matrix by the RLS approach in the present work in comparison with the prediction results by Euler-like multi-class approach. Note that the Q-$Al_3Cu_2Mg_9Si_7$ phase is selected for the modelling of precipitation and a shape parameter of $s = 0.04$ is implemented for the log-normal distribution in the RLS model.

V. CONCLUSION

A novel model termed as RLS approach which couples the Langer and Schwartz approach and log-normal particle size distribution has been developed to predict the precipitation behavior of the key precipitates including β'', β', η' in 6xxx and 7xxx Al alloys subjected to artificial aging. The available TEM and SAXS data concerning the precipitation of these secondary phases in terms of number density, mean radius, and volume fraction can be well predicted by the RLS approach. The simulation results reveal that the pre-defined log-normal size distribution in the RLS model is not fixed, where the shape parameter increases during precipitation process, corresponding to a broadening of the distribution. It is shown that the broadening of the size distribution is dependent on the magnitude of predefined shape parameter, *i.e.*, broadening is faster when a large shape parameter is used in the modelling, and vice versa. Such broadening of the particle size distribution as predicted by the present modelling is consistent with the experimental observations. Moreover, the shape parameter will also affect coarsening at later aging stage, wherein large shape parameter will lead to rapid decreasing of number density and increased growth rate of mean/critical radius. A good agreement with the Euler-like multi-class model indicates that the present RLS framework which integrates the log-normal distribution and Langer and Schwartz model is faster and equivalently accurate in precipitation prediction, and hence can serve as an efficient approach for the description of simultaneous nucleation, growth, and coarsening of the key precipitates in multi-component Al alloys during aging treatments.

ACKNOWLEDGMENTS

Open Access funding provided by NTNU Norwegian University of Science and Technology (incl St. Olavs Hospital - Trondheim University Hospital). This work is supported by the project Fundamentals of Intergranular Corrosion in Aluminium Alloys – FICAL (247598), a Knowledge Building Project for Industry co-financed by The Research Council of Norway (RCN), and the industrial partners Hydro, Gränges, Benteler, and Steertec. RCN and the industrial partners are gratefully acknowledged for their financial support.

APPENDIX

Number Density

The evolution equation of the size distribution is given by the summation of a growth term and a nucleation term:

$$\frac{\partial \phi(r)}{\partial t} = -\frac{\partial}{\partial r}(v(r)\phi(r)) + j(r) \quad [7]$$

The number density n, is defined considering only particles with radius $r > r^*$:

$$n = \int_{r^*}^{\infty} \phi(r)dr \quad [A1]$$

$$\frac{\partial n}{\partial t} = \frac{\partial}{\partial t}\left(\int_{r^*}^{\infty} \phi(r)dr\right) = -\phi(r^*)\cdot\frac{\partial r^*}{\partial t} + \int_{r^*}^{\infty}\frac{\partial \phi(r)}{\partial t}dr$$

The time derivative of the number density is obtained by combining Eqs. [7] and [A1]:

$$\frac{\partial n}{\partial t} = -\phi(r^*)\cdot\frac{\partial r^*}{\partial t} + \int_{r^*}^{\infty}\left(-\frac{\partial}{\partial r}(v(r)\phi(r)) + j(r)\right)dr \quad [A2]$$

The nucleation is assumed to form particles with radius $r^* + \Delta r^*$ only with a nucleation rate J. It means that $j(r)$ is defined as:

$$j(r) = J\cdot\delta(r^* + \Delta r^*) \quad [A3]$$

Assuming that at infinite, v and φ are zero and $v(r^*) = 0$ by definition, the equation becomes:

$$\frac{\partial n}{\partial t} = -\phi(r^*)\cdot\frac{\partial r^*}{\partial t} + \int_{r^*}^{\infty} j(r)dr \quad [A4]$$

We then obtain the final generic equation valid for any size distribution:

$$\frac{\partial n}{\partial t} = J - \phi(r^*)\cdot\frac{\partial r^*}{\partial t} \quad [8]$$

Mean Radius

The mean radius is defined by:

$$\bar{r} = \frac{1}{n}\int_{r^*}^{\infty}\phi(r)rdr \quad [9]$$

This equation is derived with time and combined with Eqs. [7] and [8]:

$$\frac{\partial \bar{r}}{\partial t} = \frac{\partial}{\partial t}\left(\frac{1}{n}\right)\int_{r^*}^{\infty}\phi(r)rdr + \frac{1}{n}\frac{\partial}{\partial t}\left(\int_{r^*}^{\infty}\phi(r)rdr\right) \quad [A5]$$

$$\frac{\partial \bar{r}}{\partial t} = -\frac{1}{n^2}\frac{\partial n}{\partial t}\int_{r^*}^{\infty}\phi(r)rdr + \frac{1}{n}\left(-\phi(r^*)\cdot r^*\cdot\frac{\partial r^*}{\partial t} + \int_{r^*}^{\infty}\frac{\partial}{\partial t}(\phi(r)r)dr\right) \quad [A6]$$

$$\frac{\partial \bar{r}}{\partial t} = -\frac{1}{n}\bar{r}\left(J - \phi(r^*)\frac{\partial r^*}{\partial t}\right) + \frac{1}{n}\left(-\phi(r^*)\cdot r^*\cdot\frac{\partial r^*}{\partial t} + \int_{r^*}^{\infty} r\frac{\partial}{\partial t}(\phi(r))dr\right) \quad [A7]$$

$$\frac{\partial \bar{r}}{\partial t} = -\frac{1}{n}\bar{r}\left(J - \phi(r^*)\frac{\partial r^*}{\partial t}\right) + \frac{1}{n}\left(-\phi(r^*)\cdot r^*\cdot\frac{\partial r^*}{\partial t} + \int_{r^*}^{\infty}\left(-r\cdot\frac{\partial}{\partial r}(v(r)\phi(r)) + r\cdot j(r)\right)dr\right) \quad [A8]$$

By applying Eq. A3 and assuming that the product r, v and φ is zero at infinite, we obtain:

$$\frac{\partial \bar{r}}{\partial t} = -\frac{1}{n}\bar{r}\left(J - \phi(r^*)\frac{\partial r^*}{\partial t}\right) + \frac{1}{n}\left(-\phi(r^*)\cdot r^* \cdot \frac{\partial r^*}{\partial t} + \int_{r^*}^{\infty} v(r)\phi(r)dr + r^* \cdot J\right) \quad [A9]$$

In the present model, we simplify the integration of $v(r)\phi(r)$ by replacing it by the growth at the mean radius, leading to the following equation:

$$\frac{\partial \bar{r}}{\partial t} = v(\bar{r}) + \frac{1}{n}(\bar{r} - r^*)\phi(r^*)\frac{\partial r^*}{\partial t} + \frac{1}{n}\cdot J \cdot (r^* + \Delta r^* - \bar{r}) \quad [10]$$

REFERENCES

1. E.A. Mørtsell, C.D. Marioara, S.J. Andersen, J. Røyset, O. Reiso, and R. Holmestad: *Metall. Mater. Trans. A*, 2015, vol. 46A, pp. 4369–79.
2. S. Wenner and R. Holmestad: *Scr. Mater.*, 2016, vol. 118, pp. 5–8.
3. E.A. Mørtsell, C.D. Marioara, S.J. Andersen, I.G. Ringdalen, J. Friis, S. Wenner, J. Røyset, O. Reiso, and R. Holmestad: *J. Alloys Compd.*, 2017, vol. 699, pp. 235–42.
4. C.D. Marioara, A. Lervik, J. Grønvold, O. Lunder, S. Wenner, T. Furu, and R. Holmestad: *Metall. Mater. Trans. A*, 2018, vol. 49A, pp. 5146–56.
5. L.P. Ding, Z.H. Jia, J.-F. Nie, Y.Y. Weng, L.F. Cao, H.W. Chen, X.Z. Wu, and Q. Liu: *Acta Mater.*, 2018, vol. 145, pp. 437–50.
6. K. Li, A. Béché, M. Song, G. Sha, X.X. Lu, K. Zhang, Y. Du, S.P. Ringer, and D. Schryvers: *Scr. Mater.*, 2014, vol. 75, pp. 86–89.
7. D.D. Zhao, L.C. Zhou, Y. Kong, A.J. Wang, J. Wang, Y.B. Peng, Y. Du, Y.F. Ouyang, and W.Q. Zhang: *J. Mater. Sci.*, 2011, vol. 46, pp. 7839–49.
8. D. Bardel, M. Perez, D. Nelias, A. Deschamps, C.R. Hutchinson, D. Maisonnette, T. Chaise, J. Garnier, and F. Bourlier: *Acta Mater.*, 2014, vol. 62, pp. 129–40.
9. M. Afshar, F.X. Mao, H.C. Jiang, V. Mohles, M. Schick, K. Hack, S. Korte-Kerzel, and L.A. Barrales-Mora: *Comput. Mater. Sci.*, 2019, vol. 158, pp. 235–42.
10. F. Qian, E.A. Mørtsell, C.D. Marioara, S.J. Andersen, and Y.J. Li: *Materialia*, 2018, vol. 4, pp. 33–37.
11. S.J. Andersen, H.W. Zandbergen, J. Jansen, C. TrÆholt, U. Tundal, and O. Reiso: *Acta Mater.*, 1998, vol. 46, pp. 3283–98.
12. A. Deschamps and Y. Brechet: *Acta Mater.*, 1999, vol. 47, pp. 293–305.
13. O.R. Myhr and Ø. Grong: *Acta Mater.*, 2000, vol. 48, pp. 1605–15.
14. O.R. Myhr, Ø. Grong, and S.J. Andersen: *Acta Mater.*, 2001, vol. 49, pp. 65–75.
15. M. Nicolas and A. Deschamps: *Acta Mater.*, 2003, vol. 51, pp. 6077–94.
16. O.R. Myhr, Ø. Grong, H.G. Fjær, and C.D. Marioara: *Acta Mater.*, 2004, vol. 52, pp. 4997–5008.
17. R. Wagner, R. Kampmann and P.W. Voorhees, *Mater. Sci. Tech.* 2006, pp. 309-407.
18. F. Perrard, A. Deschamps, and P. Maugis: *Acta Mater.*, 2007, vol. 55, pp. 1255–66.
19. M. Perez, M. Dumont, and D. Acevedo-Reyes: *Acta Mater.*, 2008, vol. 56, pp. 2119–32.
20. Q. Du, W.J. Poole, and M.A. Wells: *Acta Mater.*, 2012, vol. 60, pp. 3830–39.
21. D. den Ouden, L. Zhao, C. Vuik, J. Sietsma, and F.J. Vermolen: *Comput. Mater. Sci.*, 2013, vol. 79, pp. 933–43.
22. Z.S. Liu, V. Mohles, O. Engler, and G. Gottstein: *Comput. Mater. Sci.*, 2014, vol. 81, pp. 410–17.
23. Q. Du, B. Holmedal, J. Friis, and C.D. Marioara: *Metall. Mater. Trans. A*, 2016, vol. 47A, pp. 589–99.
24. P. Priya, D.R. Johnson, and M.J.M. Krane: *Comput. Mater. Sci.*, 2017, vol. 139, pp. 273–84.
25. Q. Du, K. Tang, C.D. Marioara, S.J. Andersen, B. Holmedal, and R. Holmestad: *Acta Mater.*, 2017, vol. 122, pp. 178–86.
26. J.S. Langer and A.J. Schwartz: *Phys. Rev. A*, 1980, vol. 21, pp. 948–58.
27. R. Kampmann and R. Wagner: *Decomposition of Alloys: The Early Stages*, Pergamon Press, Oxford, 1984, pp. 91–103.
28. P. Maugis and M. Goune: *Acta Mater.*, 2005, vol. 53, pp. 3359–67.
29. R. Kampmann, H. Eckerlebe, and R. Wagner: *Mater. Res. Soc. Symp. Proc.*, 1987, vol. 57, pp. 525–42.
30. I.M. Lifshitz and V.V. Slyozov: *J. Phys. Chem. Solids*, 1961, vol. 19, pp. 35–50.
31. M. Perez, E. Courtois, D. Acevedo, T. Epicier, and P. Maugis: *Philos. Mag. Lett.*, 2007, vol. 87, pp. 645–56.
32. J.D. Robson, M.J. Jones, and P.B. Prangnell: *Acta Mater.*, 2003, vol. 51, pp. 1453–68.
33. J.D. Robson: *Acta Mater.*, 2004, vol. 52, pp. 4669–76.
34. K.C. Russell, *Chapter Nucleation in solids* 1968, pp. 219-268.
35. C. Zener: *J. Appl. Phys.*, 1949, vol. 20, pp. 950–53.
36. M. Perez: *Scr. Mater.*, 2005, vol. 52, pp. 709–12.
37. Ch.-A. Gandin and A. Jacot: *Acta Mater.*, 2007, vol. 55, pp. 2539–53.
38. Y. Wang, Z.-K. Liu, L.-Q. Chen, and C. Wolverton: *Acta Mater.*, 2007, vol. 55, pp. 5934–47.
39. H.S. Hasting, A.G. Frøseth, S.J. Andersen, R. Vissers, J.C. Walmsley, C.D. Marioara, F. Danoix, W. Lefebvre, and R. Holmestad: *J. Appl. Phys.*, 2009, vol. 106, p. 123527.
40. R. Vissers, M.A. van Huis, J. Jansen, H.W. Zandbergen, C.D. Marioara, and S.J. Andersen: *Acta Mater.*, 2007, vol. 55, pp. 3815–23.
41. P. Donnadieu, M. Roux-Michollet, and V. Chastagnier: *Philos. Mag. A*, 1999, vol. 79, pp. 1347–66.
42. X. Fang, M. Song, K. Li, Y. Du, D.D. Zhao, C. Jiang, and H. Zhang: *J. Mater. Sci.*, 2012, vol. 47, pp. 5419–27.
43. J.H. Auld and S.M. Cousland: *J. Aust. Inst. Met.*, 1974, vol. 19, pp. 194–201.
44. C. Wolverton: *Acta Mater.*, 2001, vol. 49, pp. 3129–42.
45. F.H. Cao, J.X. Zheng, Y. Jiang, B. Chen, Y.R. Wang, and T. Hu: *Acta Mater.*, 2019, vol. 164, pp. 207–19.
46. N. Kamp, A. Sullivan, R. Tomasi, and J.D. Robson: *Acta Mater.*, 2006, vol. 54, pp. 2003–14.
47. D.M. Liu, B.Q. Xiong, F.G. Bian, Z.H. Li, X.W. Li, Y.A. Zhang, Q.S. Wang, G.L. Xie, F. Wang, and H.W. Liu: *Mater. Sci. Eng. A*, 2015, vol. 639, pp. 245–51.
48. A. Deschamps, F. Livet, and Y. Bréchet: *Acta Mater.*, 1999, vol. 47, pp. 281–92.
49. Y. Du, Y.A. Chang, B.Y. Huang, W.P. Gong, Z.P. Jin, H.H. Xu, Z.H. Yuan, Y. Liu, Y.H. He, and F.-Y. Xie: *Mater. Sci. Eng. A*, 2003, vol. 363, pp. 140–51.
50. E. Povoden-Karadeniz, P. Lang, P. Warczok, A. Falahati, W. Jun, and E. Kozeschnik: *CALPHAD*, 2013, vol. 43, pp. 94–104.
51. M.D. Jong, S.V.D. Zwaag, and M. Sluiter: *Int. J. Mater. Res.*, 2012, vol. 103, pp. 972–79.
52. K.K. Chang, S.H. Liu, D.D. Zhao, Y. Du, L.C. Zhou, and L. Chen: *Thermo. Acta*, 2011, vol. 512, pp. 258–67.